The Extra-Area Effect of Orographic Cloud Seeding: Observational Evidence of Precipitation Enhancement Downwind of the Target Mountain

XIAOQIN JING AND BART GEERTS

Department of Atmospheric Science, University of Wyoming, Laramie, Wyoming

BRUCE BOE

Weather Modification, Inc., Fargo, North Dakota

(Manuscript received 21 June 2015, in final form 6 January 2016)

ABSTRACT

This study uses scanning X-band Doppler on Wheels (DOW) radar data to examine whether ground-based glaciogenic seeding influences orographic precipitation, inadvertently, over the foothills of a mountain ~50 km downwind of the target mountain. The data were collected during seven storms during the 2012 AgI Seeding Cloud Impact Investigation (ASCII-12) campaign in Wyoming. The DOW was located on the Sierra Madre (the target range), with excellent low-level coverage toward the Medicine Bow (the downwind range). To examine the seeding impact, two study areas are designated, both over the foothills of the downwind range: one is directly downwind of the remote silver iodide (AgI) generators (target area), and the other is offset sideways (control area). Comparisons are made between radar reflectivity measurements from a treated period and those from an untreated period. The total treated (untreated) period over seven storms is 14.3 h (21.2 h). Independent measurements of ice nuclei concentrations indicate that ground-released AgI nuclei can disperse across two mountain ranges over a distance of ~80 km. Analyses of DOW transects, DOW echo-height maps, and Doppler velocities from an airborne profiling radar suggest three different mechanisms for the vertical mixing of AgI nuclei: in all cases boundary layer mixing is active, and in some cases convection, or a lee hydraulic jump, or both are present. In all cases the radar reflectivity is higher during seeding in the target region when compared with the trend over the same period in the control region. Note that the results are not definitive proof of a downwind seeding impact since natural variability of precipitation is large and the sample size examined is small.

1. Introduction

Intentional weather modification efforts normally define a target area where the impact of seeding is expected and analyzed. Usually this seeding area is within 50 km from the source of artificial nuclei (e.g., Breed et al. 2014). There have long been concerns about the downwind effect of cloud seeding activities (e.g., Long 2001; DeFelice et al. 2014). The general public often raises concerns about how precipitation enhancement in a close-fetch target area may result in less moisture in the downwind area, leading to a precipitation decrease (the "robbing Peter to pay Paul" hypothesis). Several studies have addressed this inadvertent downwind effect (e.g., Long 2001; Solak et al. 2003; Griffith et al. 2005; Wise 2005), often referred to as an "extra area" effect (DeFelice et al. 2014). Much effort has been devoted to understanding the seeding-induced changes of cloud microphysics and precipitation at close range (e.g., Manton et al. 2011; B. Pokharel et al. 2015, manuscript submitted to *J. Appl. Meteor. Climatol.*). The extra-area effect of cloud seeding is a more complicated problem compared to that at a close range, involving the dispersion, transport, and (possibly multiple) cloud microphysical transformations of seeding material over a long range. The effect is important because of unintended consequences on the regional water cycle. A solid understanding of the extra-area effect remains elusive, which is not surprising given that the impact of seeding within the target area itself is difficult to ascertain (e.g., Geerts et al. 2010, 2013; Pokharel et al. 2014a,b; Chu et al. 2014).

Both observational and modeling studies have shown that dispersion plumes of seeding material may extend long distances downwind from their source. For

Corresponding author address: Xiaoqin Jing, Dept. of Atmospheric Science, University of Wyoming, Laramie, WY 82071.
E-mail: xjing@uwyo.edu

DOI: 10.1175/JAMC-D-15-0188.1

example, Mulvey (1977) analyzed the observations of airborne ice nuclei (IN) concentration and surface silver concentration in freshly fallen snow, and showed that the silver iodide (AgI) seeding material could be transported at least 130 km downwind of the primary target area. Boe et al. (2014) studied the dispersion of AgI nuclei produced by ground-based generators; they observed high concentrations of IN about 100 km downwind of the AgI generators, and found that AgI nuclei can linger across this distance for more than 2 h after seeding has stopped. Recent WRF simulations [as mentioned in the Weather Modification Pilot Program Executive Summary (Wyoming Water Development Commission 2014)] show that ground-based seeding material can be transported several hundred kilometers downstream (L. Xue 2015, personal communication).

Some studies have suggested that precipitation in the extra area may be enhanced during periods of upwind seeding. A National Science Foundation sponsored workshop conducted in August 1977 summarized some early studies of the extra-area effect and reported that "the 'better quality' evidence available from mostly a-posteriori analyses of randomized seeding programs suggests that precipitation changes in extended areas tends to be similar in sign (i.e., increases or decreases) and roughly the same magnitude as those in the primary 'target area'. The extended effects appear to be detectable at distances of a few hundred kilometers from the seeding source" (DeFelice et al. 2014). New measurement capabilities have allowed a more comprehensive analysis of the extra-area seeding effect since then. Solak et al. (2003) analyzed the data collected from a long-term cloud seeding program conducted in Utah (25 winter seasons in total), and found a positive extra-area effect out to 200 km, with an average precipitation increase of about 8%. Griffith et al. (2009) examined the results of long-term randomized research and operational cloud seeding activities and found that precipitation enhancement can extend 150 km downwind of the seeding sources. Recently, Hunter (2009) summarized 28 studies based on field experiments conducted between 1971 and 2006. The preponderance of studies in this survey indicate that the AgI nuclei can remain active for many hours and can be transported to areas remote from the intended target areas, where the nuclei can facilitate ice initiation and thus may enhance precipitation.

Most of the surveyed studies examine surface precipitation statistics only and lack the high-density observations (e.g., high-resolution radar or aircraft data) needed to gain a better understanding of the physical processes. Hunter (2009) points to a need for more detailed observational evidence.

The present study uses the Doppler on Wheels (DOW), a high-resolution scanning X-band (3 cm) Doppler radar, to examine observational evidence of an extra-area seeding effect downwind of the primary target mountain. The DOW operated as one of the main instruments in the 2012 AgI Seeding Cloud Impact Investigation (ASCII-12) campaign, conducted over the Sierra Madre Range in Wyoming (Geerts et al. 2013). The original objectives of ASCII did not include the study of extra-area effects; however, the excellent low-level DOW coverage along the foothills of a downwind mountain (Medicine Bow Range) ~50 km away provides a unique opportunity to assess precipitation changes downwind of the target area.

This study uses the data collected from seven ASCII-12 intensive observation periods (IOPs). Section 2 introduces the experimental design and instruments. Section 3 presents the analysis method. Atmospheric characteristics of the seven cases are described in section 4. Section 5 explores the extra-area seeding effect. Section 6 discusses the main findings and the uncertainties. Conclusions are given in section 7.

2. Experimental design and instrumentation

The ASCII-12 campaign was conducted from January to March 2012 over the Sierra Madre in southern Wyoming (Fig. 1). The low-level flow typically was southwesterly or westerly during ASCII-12 IOPs, supercooled liquid water was commonly observed in clouds over the Sierra Madre, and snowfall occurred frequently (Geerts et al. 2013). The upstream environment was characterized by GPS Advanced Upper-Air Sounding (GAUS) rawinsondes, launched about every 2 h in each IOP from Dixon, Wyoming (Fig. 1b). The liquid water path (LWP) was measured by a dual-frequency passive microwave radiometer (Geerts et al. 2013). An acoustic ice nucleus counter (AINC) was operated at Mountain Meadow Cabins (MMC), also shown in Fig. 1b. The University of Wyoming King Air (UWKA) carried a profiling millimeter-wave Doppler radar, the Wyoming Cloud Radar (WCR). This radar has been used as a key instrument in several ASCII studies (e.g., Geerts et al. 2010, 2013; Pokharel et al. 2014a,b) but plays only a peripheral role here. The vertical transects of WCR reflectivity and vertical velocity from along-wind flight tracks are used to explore the vertical structure of precipitation, flow, and turbulence across the Sierra Madre. Several other instruments, such as Micro Rain Radars (MRRs) and snow gauges, were also operated in the field campaign but not used in this study. More detailed information of the ASCII-12 experimental design and instruments can be found in Geerts et al. (2013).

This study is based primarily on data collected by the DOW, a dual-polarization X-band Doppler radar. In

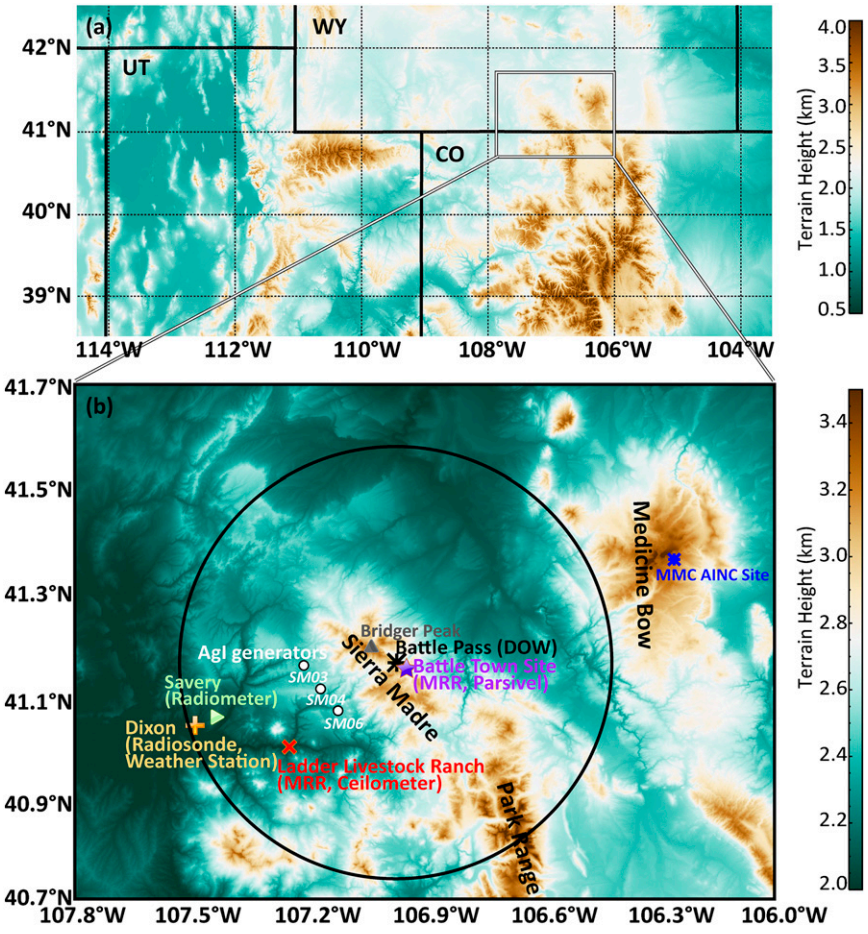

FIG. 1. ASCII experimental design map. (a) The topography of the surrounding region, with a box showing the location of this experiment. (b) A zoomed-in view within this box, with terrain height as the background color field. The DOW radar is located at Battle Pass (black asterisk). The big black circle shows the DOW detection range. The small white circles show the locations of the AgI generators (SM*nn*). Several other instrument sites over and upwind of the Sierra Madre and Medicine Bow are also shown.

ASCII-12 this radar operated with a maximum range of 48 km (Fig. 1b) and completed a full-volume scan every ~10 min, including 41 plan position indicator (PPI) scans from −1° to 85° elevation, and six range–height indicator (RHI) scans (Jing et al. 2015). The DOW was located at Battle Pass during ASCII-12, which allowed for low-elevation radar coverage downwind of the AgI generators to the east and northeast. The lowest PPI scan (−1°) was unblocked in a wide window in those directions (Fig. 2a). Battle Pass is surrounded by higher terrain to the northwest and southeast, resulting in a lack of low-level radar coverage in those directions. More detailed information related to the DOWs and the data processing for ASCII-12 can be found in Jing et al. (2015).

The maximum range of DOW data is sufficient to examine echoes 50–70 km downwind of the AgI generators (Fig. 1b). The DOW operated in 12 IOPs during ASCII-12. One of them (IOP 4) is excluded because of a total lack of radar echoes downwind of the Sierra Madre, and another (IOP 10) is excluded because of a frontal passage. The other 10 IOPs can be used to study the seeding impact. In three of them, eight AgI generators were operated in a broad area upwind of the Sierra Madre (Breed et al. 2014). For the remaining seven IOPs, a cluster of three generators was operated (Fig. 1b). To study the extra-area seeding effect, we compare the radar returns over the foothills of the Medicine Bow Range (downwind range) directly downstream of this cluster of generators to the radar echoes above an adjacent area in the same foothills. The reason is that precipitation is a highly variable field, trending rapidly over the course of a few hours, so a simple temporal trend in the region directly downstream of generators (the inadvertent target region, for

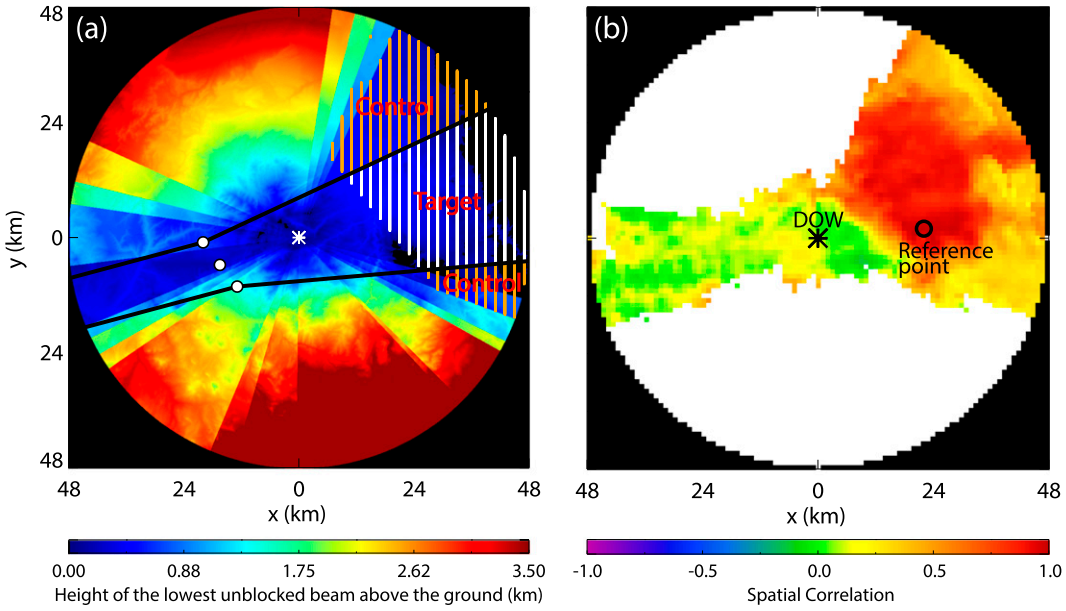

FIG. 2. (a) Height (km AGL) of the lowest unblocked DOW beam. The vertical hatchings show the locations of the control area (orange) and the target area (white) downwind of the Sierra Madre. The boundaries separating these areas (black lines) pivot with the wind direction. (This example applies to IOP 9.) The black lines upstream of the AgI generators show the IOP-specific mean wind direction, and those downstream of the generators are rotated out by ±10°. (b) Spatial autocorrelation of the snow rate calculated based on mean low-level reflectivity for a reference point in the lee of the Sierra Madre.

the purpose of this study) is not sufficient to demonstrate a seeding effect. Instead, this trend must be compared to that in an adjacent area (the control region) to show the overall impact. The AgI plumes produced by the broad network of eight generators will cover the whole Medicine Bow foothills region scanned by the DOW, which makes it impossible to designate a control area. Therefore, only the seven IOPs with three AgI generators are used in this paper. Further details of these regions and the analysis method are presented in section 3.

3. Analysis method

The analysis method used for this study is similar to that in Jing et al. (2015); the following summarizes that method and highlights modifications specific to this study.

To assess possible extra-area seeding impacts, two regions are designated (Fig. 2a), both over the foothills of the downwind range. The *target area* is directly downwind of the remote AgI generators, with the *control area* offset sideways. The control area is designed to be unaffected or less affected by the AgI seeding, while the target area is more affected by seeding. The terms less and more affected are used here because the AgI plume dispersion patterns are not known. Previous studies suggest AgI seeding plumes tend to be rather narrow, including both observational studies (Huggins 2007; Holroyd et al. 1988) and modeling work (Chu et al. 2014). This led us to use a dispersion angle of ±10°, starting at the cluster of AgI generators (Fig. 2). Areas outside this dispersion angle are assumed to be unaffected or less affected by AgI seeding (control), and the area inside the cone is considered to be the target region. The southwestern boundary of the target and control region is the valley floor between the Sierra Madre and the Medicine Bow Ranges, and the northeastern boundary is the DOW's maximum range. The other boundaries of the study areas (e.g., the northern or southern boundaries of the control area) are defined by the requirement that the lowest unblocked DOW beam is no more than 1.0 km above ground level (AGL). This 1.0 km AGL threshold is chosen because the low-level precipitation, mainly within the planetary boundary layer (PBL), is of primary importance in terms of the ground-based seeding effect.

The target and control regions are slightly different in the various IOPs as a result of the differing mean wind directions. In IOPs 5 and 16, the control area is to the south of the target area, while in IOPs 8, 12, and 14, the control area is to the north of the target area. In IOPs 9 and 13, the control area is split into two parts on opposite sides of the target area.

In each IOP, the DOW reflectivity change from an untreated period (NOSEED) to a treated period (SEED) is analyzed. The NOSEED and SEED time

TABLE 1. Summary of the seven IOPs. Shown are the start times of the first and last DOW volume scans included in the NOSEED and SEED periods, the time delay used for certain regions, and the sequence of NOSEED and SEED periods. The duration of each period (h) is shown in parentheses in the NOSEED and SEED columns. They are in 10-min increments—the period of the DOW measurement cycle— and are estimated based on the distance from the three AgI generators, and the average wind speed shown in Table 2.

ASCII IOP	Date	NOSEED start–end	SEED start–end time (UTC)	Time delay (min)	Sequence
5	19 Jan 2012	1433–1852 (4.2)	1852–2051 (2.0)	40	NOSEED then SEED
8	12 Feb 2012	0511–0836 (3.5)	2347–0341 (3.9)	100	SEED then NOSEED
9	13 Feb 2012	1831–2220 (3.8)	2220–2309 (0.8)	120	NOSEED then SEED
12	22 Feb 2012	1318–1551 (2.5)	1551–1752 (2.0)	40	NOSEED then SEED
13	28 Feb 2012a	1309–1614 (3.0)	1614–1745 (1.5)	60	NOSEED then SEED
14	28 Feb 2012b	1906–2139 (2.5)	2139–2340 (2.0)	50	NOSEED then SEED
16	29 Feb 2012	0201–0342 (1.7)	2230–0039 (2.1)	40	SEED then NOSEED

periods for the seven IOPs are shown in Table 1. These time periods are not the same as the start-to-end times of the AgI generators because of the transport time of the AgI nuclei. Based on the mean low-level wind speed, the delay in the NOSEED–SEED times for these IOPs ranged from 40 to 120 min. In five cases (IOPs 5, 9, 12, 13, and 14) the NOSEED period is followed by the SEED periods, while in IOPs 8 and 16 the SEED period precedes the NOSEED period. The latter requires a buffer period between cases (~1.5 h) because of the lingering presence of AgI nuclei (e.g., Holroyd et al. 1988; Boe et al. 2014).

The temporal changes (SEED − NOSEED) in reflectivity observed by the DOW in the target and control regions are compared to assess the seeding impact. This double-difference method, in time and space, has been used elsewhere (e.g., Gabriel 1999; Pokharel et al. 2014a; Jing et al. 2015). It builds on the basic assumption that the natural trend in cloud and precipitation properties is about the same in the control and target areas. To assess this, we examine the spatial autocorrelation of the snow rate (S), estimated from the 0–1.5-km mean reflectivity (Z) at any 1 km × 1 km grid box using $Z = 100S^{1.5}$ (Z in mm^6 m^{-3}, S in mm h^{-1} water equivalent) (Matrosov et al. 2009), based on the seven IOPs with DOW data during the NOSEED period. The spatial autocorrelation map at the reference point shown in Fig. 2b, or at any other select point downwind of the Sierra Madre, shows that precipitation east of the Sierra Madre is strongly correlated, but aligns weakly with the precipitation across the Sierra Madre itself. The correlation between the control and target regions (illustrated in Fig. 2a) is high: the area-average values exceed 0.8 for each IOP, suggesting the storm evolution is similar between the two regions.

The duration of the sampling period is also important (Jing et al. 2015). In most of the IOPs, the AgI generators released AgI nuclei for more than 2 h, but often the DOW did not operate for the full duration of seeding. Therefore, the extra-area SEED periods often are shorter than the AgI seeding periods. They are further reduced to account for the time needed for the downwind AgI transport, resulting in a rather short SEED period in some cases (e.g., IOP 9; see Table 1).

Finally, we note that the DOW was calibrated in each IOP and showed a typical temporal drift in reflectivity of about 0.1 dB in each IOP (Jing et al. 2015). Although the double-difference approach should remove this drift, it is fair to say that the seeding impact uncertainty related to the radar is ~0.1 dB.

4. Characteristics of the seven IOPs used in this study

a. *Ambient weather conditions*

The upstream weather conditions of the seven IOPs used in this study are summarized in Table 2. Most of this information is derived from the soundings released from Dixon (Fig. 1b), that is, upwind of the Sierra Madre Range (not just the Medicine Bow Range). The temperature at 700 hPa is listed because this represents the average pressure of the DOW site at Battle Pass. The 700-hPa temperature varied from −9.5° to −2.6°C (Table 2). Assuming mixing over at least ~500 m, which is the minimum mixing depth according to the WCR data analyzed in Geerts et al. (2013), in-cloud temperatures should be cold enough for AgI nuclei to initiate ice in cloud (Breed et al. 2014).

The low-level wind was generally greater than 15 m s^{-1} and roughly westerly, except for IOPs 8 and 9 when the wind was relatively weak. The bulk Froude number (Fr) exceeded unity even for those two weak-wind cases, because the Brunt–Väisälä (B–V) frequency N was generally small[1] (Table 2). This indicates that the upwind low-level

[1] The value for N is a weighted average of the dry B–V frequency, calculated between the surface and cloud base [i.e., lifting condensation level (LCL)], and the moist B–V frequency, calculated between the LCL and the height of Bridger Peak, the highest point in the Sierra Madre Range.

TABLE 2. Summary of the upstream environment for the seven IOPs. Most of the information in this table is derived from a series of radiosondes released from Dixon (Fig. 1b) during the IOPs. Average values are calculated based on three soundings each. The Froude number (Fr) is calculated as the wind speed divided by the B–V frequency N and the height of Bridger Peak above Dixon. The LWP is inferred from a passive microwave radiometer at Savery, and the downwind properties come from the DOW and/or WCR.

			Avg from surface to Bridger Peak elev (3354 m)						
ASCII IOP	700-hPa T (°C)	LCL T (°C)	Alt (m MSL)	Speed (m s^{-1})	Direction (°)	N (10^{-2} s^{-1})	Fr	LWP (10^{-2} mm)	Downwind properties
5	−2.6	−4.9	3331	18.9	237	0.88	1.7	15	Stratiform patchy
8	−5.9	−3.9	2471	7.7	279	0.52	1.5	2	Convection, hydraulic jump?
9	−8.2	−4.2	2418	5.1	249	0.32	1.7	3	Shallow convection
12	−4.6	−3.2	2870	20.5	260	0.84	2.0	31	Stratiform patchy
13	−7.2	−4.0	2336	12.9	242	0.34	3.1	17	Stratiform, hydraulic jump
14	−9.1	−6.5	2624	15.3	283	0.27	5.1	7	Shallow convection
16	−9.5	−9.8	3012	18.3	213	0.49	3.1	12	Few, weak echoes

air, including the AgI plumes, is advected across the Sierra Madre Range. The low-level wind direction and the presence of silver in freshly fallen snow (B. Pokharel et al. 2015, manuscript submitted to *J. Appl. Meteor. Climatol.*) at the Battle Town site (Fig. 1b) indicate that the AgI plume from at least one of the three AgI generators was advected across Battle Pass during each of the IOPs.

Supercooled liquid water (SLW) was present in all cases, according to flight-level (not shown) and microwave radiometer data (Table 2), although not in large quantities. The radiometer at Savery, Wyoming (Fig. 1b), was pointed toward the Sierra Madre Range at a low angle just above the horizon. Radiometer LWP values were less than 0.1 mm for IOPs 8, 9, and 14. This may be too low for effective cloud seeding (Hashimoto et al. 2008; Manton et al. 2011), although in all three cases convective clouds were present, and the peak LWP values (presumably representing those clouds) exceeded 0.1 mm.

The precipitation downwind of the Sierra Madre Range is characterized using DOW low-elevation reflectivity maps, DOW RHI scans, and WCR reflectivity and vertical velocity transects. This characterization is summarized in the last column of Table 2. No WCR data were collected for IOPs 5 and 8. In two of the seven IOPs shallow convection (<2 km deep) was present. An example of WCR transects for a shallow convective case (IOP 9) can be found in Pokharel et al. (2014b), and another such example for a shallow stratiform case with large supercooled droplets (IOP12) is discussed in Pokharel et al. (2015). In most cases the cloud top was rather low over the terrain. Relatively deep convection (~5 km deep) was present in IOP 8. In IOP 13, strong downslope winds were documented by the WCR in the lee of the Sierra Madre, followed by a hydraulic jump with a strong updraft at flight level (~1.8 km AGL; not shown).

Several examples of hydraulic jumps in the lee of the Medicine Bow Range are shown in Chu et al. (2014) and Geerts et al. (2015). No along-wind UWKA track was flown during IOP 8, but the DOW radial velocities indicated strong downslope winds with a sudden deceleration at approximately 15–20 km downwind of Battle Pass in this case (not shown). This convergence suggests a hydraulic jump; hence, it is listed in Table 2 with a question mark. Both convection and hydraulic jumps may mix ground-released AgI nuclei from the boundary layer into the free atmosphere, as discussed below.

b. *Possible mechanisms for the vertical mixing of AgI nuclei into the extra area*

In general, concentrations of ground-released AgI nuclei decrease rapidly with height, according to observations (Boe et al. 2014) and modeling work (Xue et al. 2014). PBL mixing is the key mechanism for the dispersion of AgI nuclei from the ground into orographic clouds (e.g., Chu et al. 2014). Several studies of ground-based cloud seeding have shown that the seeding impact is mostly confined to the boundary layer (e.g., Geerts et al. 2010; Pokharel et al. 2014a,b, 2015; Jing et al. 2015).

Two other mechanisms may result in deeper mixing of the AgI particles, which may impact ice initiation over the downwind range. The first one is convection. An example of a DOW RHI scan through convective cells is shown in Fig. 3a. In this case, >20 dBZ convective cores reached as high as ~3 km AGL. Two other IOPs (IOPs 9 and 14) reveal convection downwind of the Sierra Madre, although they were shallower and weaker (Table 2).

The second mechanism is a hydraulic jump in the lee of the mountain range (Table 2). An example is shown in Fig. 3a: the radar echo weakened from the crest to the lee, and the radial velocity between this weakening echo and the more intense echoes farther downwind suggests a 9 m s^{-1} convergence. Cells had weakened 2 h later (Fig. 3b), but echo tops again subsided from the crest to near the surface about 10 km east of the DOW, and the radial velocities indicate an even stronger convergence (~11 m s^{-1}). The first significant downwind echo (labeled A in Fig. 3b) starts at ~26 km east of the crest at a height of 2–3 km AGL, which is deeper than

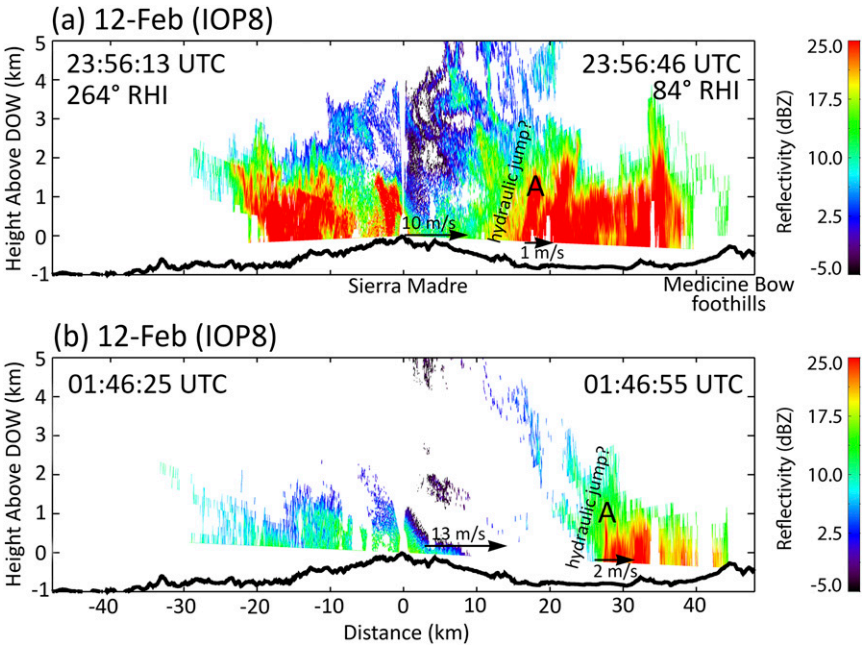

FIG. 3. Examples of DOW RHI scans oriented approximately along the wind from left to right from IOP 8. The thick black line shows the underlying terrain. The DOW is located at $x = 0$. Arrows are shown to highlight notable changes in DOW radial velocity.

the PBL. This first echo may have been initiated by a hydraulic jump. Similar sharp, elevated leading edges of precipitation were fairly persistent in IOPs 8 and 13, although not in exactly the same location.

The 5-dBZ DOW echo-top-height maps for all seven cases are shown in Fig. 4. These maps are constructed by populating the gridded volume with reflectivity values in each IOP, for all volume scans, and then averaging the values for each grid cell. First, these maps confirm that most storms are relatively shallow, especially considering the height of the terrain, over 2 km MSL (Fig. 1). Second, the spatial distribution of DOW echo tops gives some insights into precipitation mechanisms. In IOPs 8 and 13, the deepest echoes tend to occur downwind of the Sierra Madre in bands roughly aligned with the mountain crest, suggesting a quasi-stationary hydraulic jump initiating moderately deep convection (Fig. 3). Small convective cells are observed during IOPs 9 and 14. Neither convection nor a hydraulic jump is present in IOPs 5, 12, and 16; thus, PBL mixing is probably the primary mechanism for AgI mixing.

5. Exploring an inadvertent seeding signature

a. Observational evidence of AgI nuclei in the extra area

As mentioned before, ASCII-12 was not designed to study an extra-area effect. Thus, we do not have any enhanced measurements over the Medicine Bow Range during the field campaign, which was centered over the Sierra Madre (Fig. 1b). However, from 2008 to 2011, a ground-based AINC was operated in the Medicine Bow Range to study the dispersion of AgI as part of the Wyoming Weather Modification Pilot Project (WWMPP; Breed et al. 2014), which provides some evidence of AgI downwind contamination.

The AINC consists of a cloud chamber, cooled to −18°C, into which sample air is drawn at approximately 10 L min^{-1}. Before the sample air goes into the cloud chamber, it passes through a humidifier containing heavy felt wetted with distilled water at approximately +20°C to enrich the moisture content. Sodium chloride (NaCl) cloud condensation nuclei (CCN) produced by an atomizer are also added to the sample-laden, humidified air, which then flows into the cloud chamber. The chamber temperature is maintained at −18°C, cold enough to generate ice particles nucleated from AgI (DeMott 1997). These ice particles then grow to a detectable size (20 μm in diameter), and rapidly accelerate as they pass through a glass Venturi tube, producing an audible click sound.The clicks or ''counts'' are summed and recorded at 1-Hz frequency (Boe et al. 2014). Unlike AgI nuclei, most natural IN activates at significantly lower temperatures, and often do not have enough time to grow to detectable sizes in the AINC chamber. To verify that this is indeed the case in the Medicine Bow Range, the ground-based AINC was

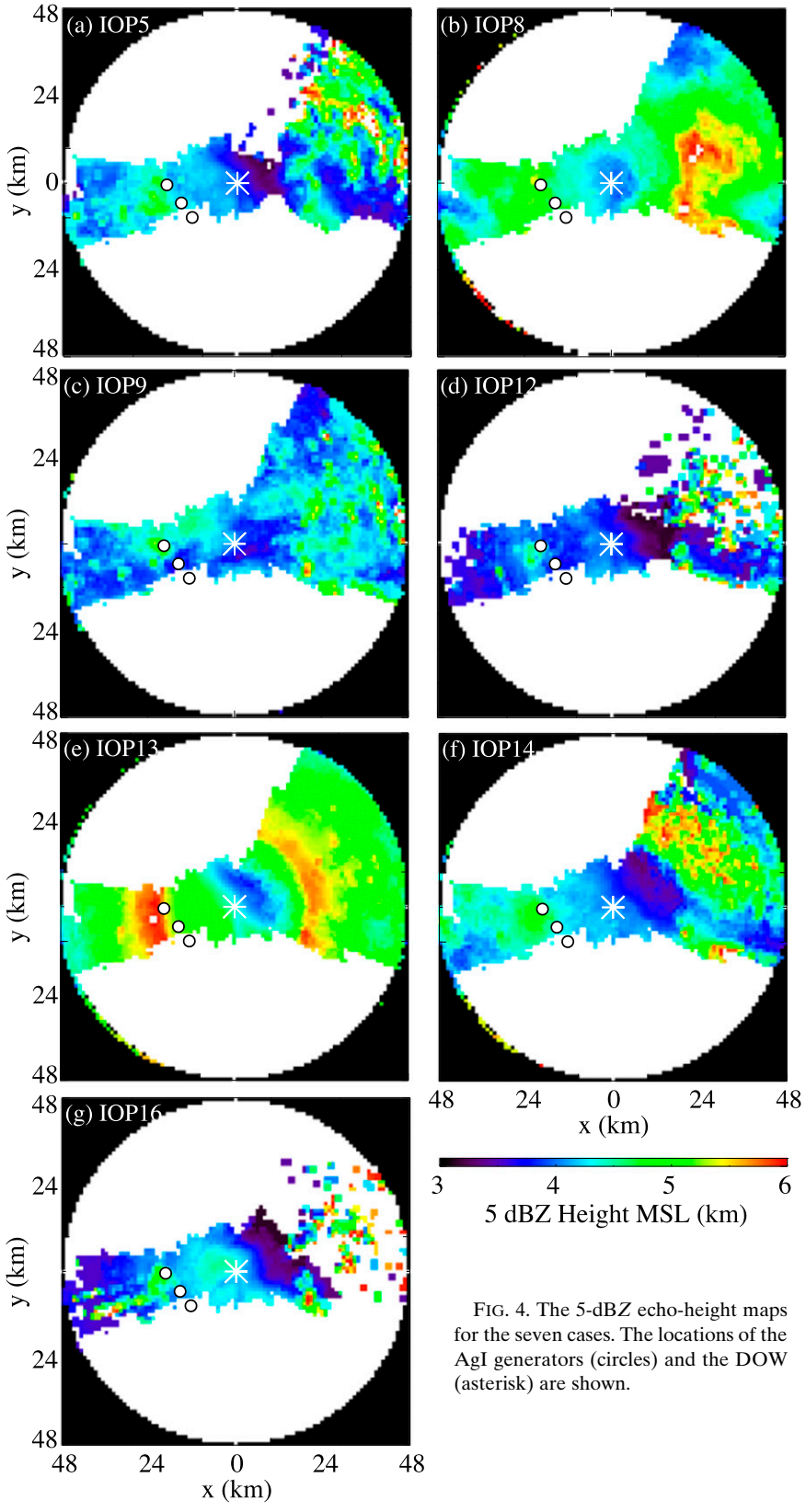

FIG. 4. The 5-dBZ echo-height maps for the seven cases. The locations of the AgI generators (circles) and the DOW (asterisk) are shown.

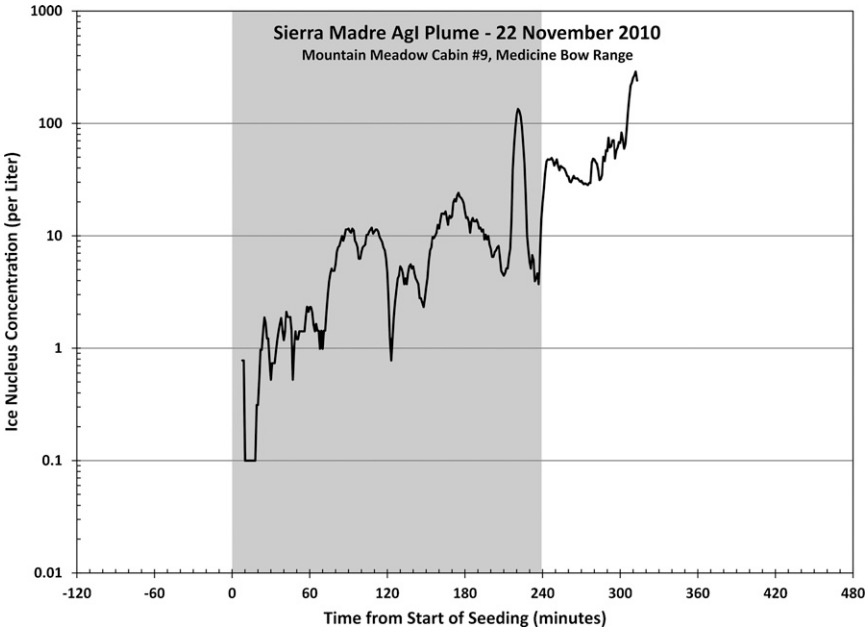

FIG. 5. The IN concentration measured by a ground-based acoustic IN counter located at MMC in the Medicine Bow Range (Fig. 1b) on 22 Nov 2010. The gray zone highlights the seeding period upwind of the Sierra Madre.

operated at −18°C for many hours in the absence of seeding during several winters (2008–11). The results show the natural IN concentration was observed to be less than 0.1 L^{-1} (Boe et al. 2014). Thus, it is reasonable to attribute the observed high IN concentration to AgI dispersion.

A clear example of downwind AgI contamination is shown in Fig. 5. On this day, 22 November 2010, snowfall was recorded over both mountain ranges, and the Sierra Madre was targeted as a seeding case in the WWMPP. Data from a radiosonde released from Saratoga (located between the two mountain ranges) just before the start of this event show strong low- level winds from ~250°, which corresponds with the alignment between the Sierra Madre generators and the AINC in the Medicine Bow Range (Fig. 1b). The IN concentration measured by the AINC at MMC steadily increased in this example, starting about 30 min after the AgI generators over the Sierra Madre (~90 km upwind) were activated, and they remained high until the end of the measurement period, ~75 min after seeding ceased. The radiosonde-derived low-level wind (average between the surface and mountaintop level) suggests a mean advection time from the source to MMC of ~80 min, so it is not implausible that the peak IN concentration was observed toward the end of the measurement period (Fig. 5). Downwind contamination was likely in several other WWMPP cases, in addition to the 22 November 2010 case, as reported in the WWMPP (Wyoming Water Development Commission 2014). The word contamination is used here because the WWMPP experimental design considered the two mountains to be independent, even when serially aligned (Breed et al. 2014).

b. *Changes in radar reflectivity*

In this section we use frequency-by-altitude diagrams (FADs; Yuter and Houze 1995) of DOW reflectivity to examine the possible seeding-induced changes in precipitation rate (Fig. 6). Equivalent reflectivity Z ($mm^6\,m^{-3}$) correlates reasonably well with precipitation rate S ($mm\,h^{-1}$), especially for the light precipitation rate typically observed during the IOPs studied here. Since the isentropes and PBL depth generally follow the terrain, the heights in the FAD diagrams are expressed as being above local ground level. The resolution of the radar reflectivity in each FAD is 0.5 dBZ, and the resolution of height is 100 m. Each level is normalized individually. The "data presence" (yellow line in Fig. 6), calculated as the area with radar echoes divided by the total area in the control and target regions at each level, tends to decrease with height, indicating fewer radar echoes at higher levels, and the clouds are relatively shallow in some cases.

All seven cases are composited in Fig. 6. The full composite is partitioned into two periods (SEED and NOSEED, defined in Table 1) and two regions (control and target, defined in section 3). In both the target and control regions, Z tends to increase toward the cloud base, indicating growth of the precipitating particles (Fig. 6). Below the cloud base, Z decreases to the ground or remains of similar magnitude. In the lowest few 100 m

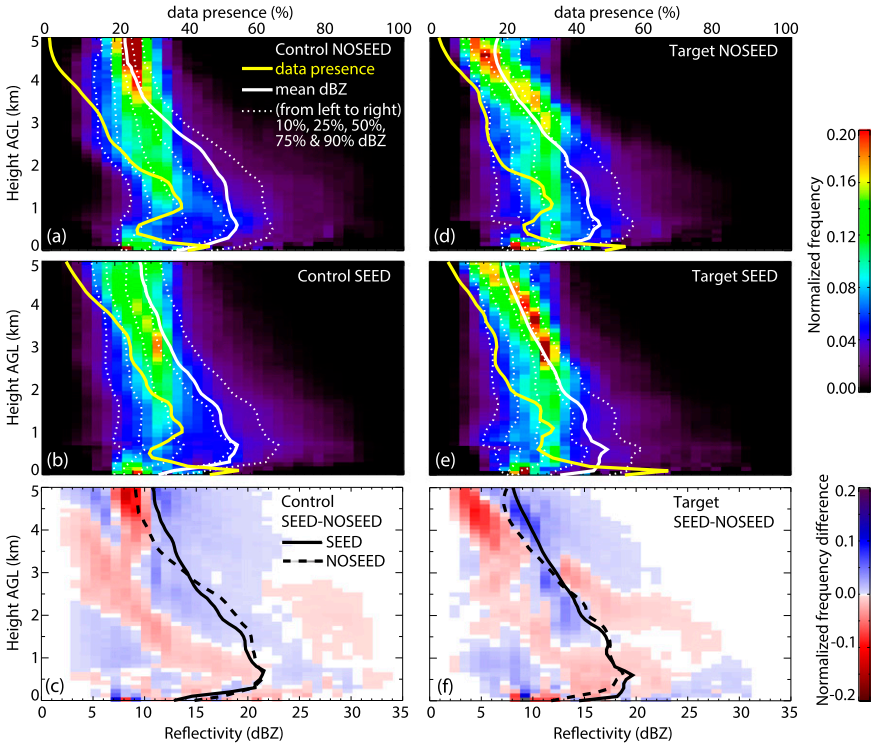

FIG. 6. Composite normalized FADs of DOW reflectivity above local ground level for the seven cases, showing the (a),(d) NOSEED and (b),(e) SEED periods and (c),(f) the difference (SEED − NOSEED) for the (left) control and (right) target regions. The average reflectivity profiles are shown as white solid lines in (a), (b), (d), and (e) and as black lines in (c) and (f). Also, in (a), (b), (d), and (e) the data presence of the NOSEED and SEED periods for the two areas is shown as yellow lines and the 10%, 25%, 50%, 75%, and 90% reflectivity values are shown as the white dotted lines.

AGL, the data quality is dubious because of a lack of echoes. Figures 6c and 6f show the *temporal* changes in reflectivity frequency for the control and target regions (SEED − NOSEED). In the control area, the mean low-level Z (white lines) decreases by ~1 dB during SEED, suggesting weaker precipitation. At high levels, the average Z is larger during SEED, suggesting natural cloud deepening. This deepening is also observed in the target area, yet the mean low-level Z increases by 2 dB (Fig. 6f). The colored frequency distribution in Fig. 6f presents obvious dipoles at high level, with blue dominating the right and red dominating the left, suggesting storm intensification. Near the surface, the frequency of high reflectivity increases in the target area, while there is no big change in the control area. *This temporal difference in the target area (compared to the control area) suggests that seeding increases precipitation over a downwind range*. It is possible that the enhanced Z aloft (above the PBL) in the target area during SEED also is affected by seeding, as convection and/or a hydraulic jump may loft AgI nuclei above the PBL (section 4b). The 10%, 25%, 50%, 75%, and 90% values of reflectivity, shown by the white dotted lines in Figs. 6a, 6b, 6d, and 6e, indicate that the enhancement of low-level mean reflectivity in the target area is mainly due to an increase in high-reflectivity values, because the 90% line increases in the target area relative to that in the control area while the 10%, 25%, 50%, and 75% lines hardly change.

The 3D structure of the reflectivity difference (SEED − NOSEED) is mapped in Fig. 7. Here, the seven cases are partitioned into three groups on the basis of wind direction: the first group (Fig. 7a) represents the cases with mostly southwest flow and thus a control area located to the south of the target area (IOPs 5 and 16), the second group (Fig. 7b) represents the cases with mostly northwest flow and a control area to the north of the target area (IOPs 8, 12, and 14), and the third group (Fig. 7c) represents the remaining cases with west flow and the control area straddling the target area on two sides (IOPs 9 and 13). The positive (blue) area tends to shift from north to south as the wind shifts from southwest (Fig. 7a) to northwest (Fig. 7b), mainly at low levels; in other words, *the positive extra-area seeding effect shifts with wind direction*, as one intuitively expects.

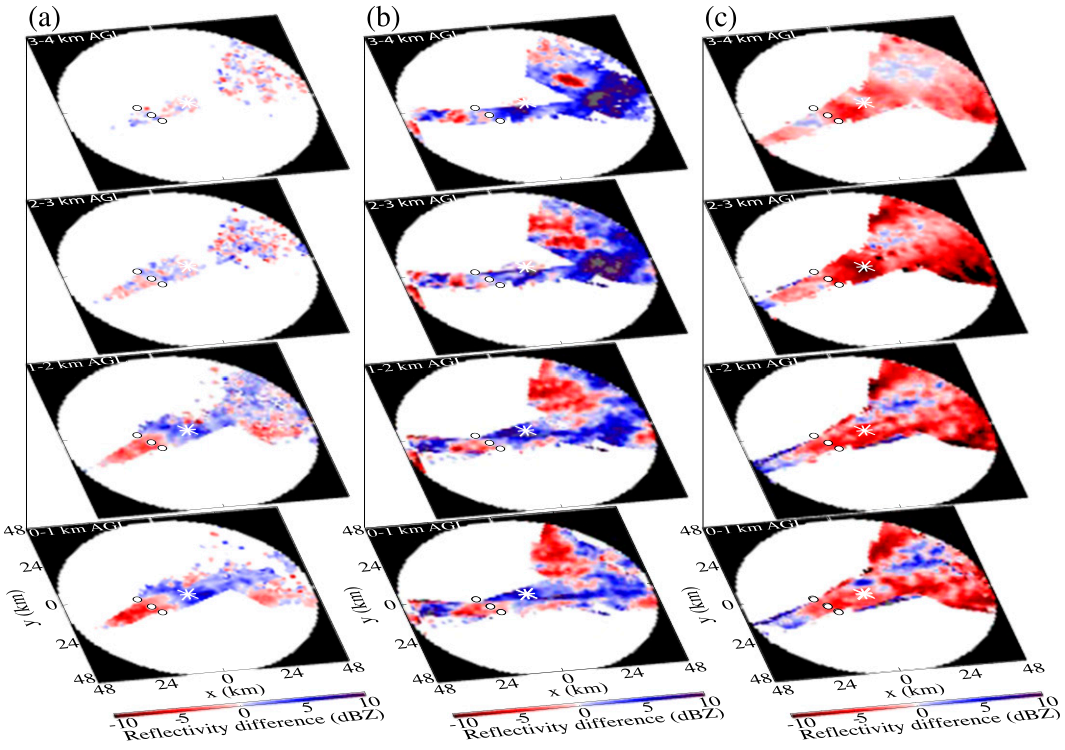

FIG. 7. Composite reflectivity difference (SEED − NOSEED) maps for (bottom) 0–1, (bottom middle) 1–2, (top middle) 2–3, and (top) 3–4 km AGL. Cases are separated on the basis of wind directions, grouping cases in which the control area is located (a) mainly to the south (IOPs 5 and 16), (b) mainly to the north (IOPs 8, 12, and 14), and (c) on both sides (IOPs 9 and 13) of the target area, respectively.

In both IOPs in the first group (Fig. 7a) PBL mixing is probably the only AgI mixing mechanism; thus, the expected seeding impact is confined to low levels, as is the case (Fig. 7a). The second group (Fig. 7b) is dominated by two cases with convection and/or a hydraulic jump (IOPs 8 and 14; Table 2), suggesting deeper AgI mixing and a stronger extra-area seeding effect. Indeed, Fig. 7b reveals a deeper (up to ~4 km AGL) Z increase in the target area; in fact, the Z increase is largest aloft. The two storms composing the third group (Fig. 7c) experienced opposite trends: natural weakening occurred during SEED in IOP 13, whereas strengthening occurred during IOP 9. The average Z maps in Fig. 7c show that the negative trend dominated; however, some low-level reflectivity increase can be seen directly downwind of the AgI generators.

c. *Isolating a seeding signature: Double ratio*

To tease out the possible seeding impact and examine its vertical reach, we use the Z impact parameter (ZIP), which has been used in several other studies (e.g., Gabriel 1999; Pokharel et al. 2014a,b; Chu et al. 2014). Here, ZIP is defined as the difference between the Z change in a target area and that in the corresponding control area:

$$\mathrm{ZIP} = \Delta \mathrm{dB}Z_T - \Delta \mathrm{dB}Z_C, \tag{1}$$

where $\Delta \mathrm{dB}Z = \mathrm{dB}Z_{\mathrm{SEED}} - \mathrm{dB}Z_{\mathrm{NOSEED}}$ and the subscripts T and C refer to target and control, respectively.

The profiles of ZIP are shown in Fig. 8. The main message from Fig. 8 is that in all the IOPs, ZIP is positive below ~1 km AGL. This suggests *a positive impact of seeding on surface precipitation over the downwind mountain range in each of the seven cases*. Note that the sample size in IOP 16 is very small. In IOPs 8 and 13, positive ZIP values are found from near the surface up to ~4 km AGL, possibly because of the relatively deep convection and/or hydraulic jump in the lee of the Sierra Madre (Fig. 3). Convection is present during IOPs 9 and 14, but it is relatively shallow, so the AgI mixing and positive ZIP values are not expected to be deep. For IOPs 5, 12, and 16, without convection or hydraulic jump, positive ZIP values are present at low levels.

d. *Uncertainty of seeding impact derived from ZIP*

We now aim to ascertain the level of confidence in the finding stated in section 5c. As mentioned before, the basic assumption in using ZIP as an indicator of seeding impact is that the natural trends are the same in the control and

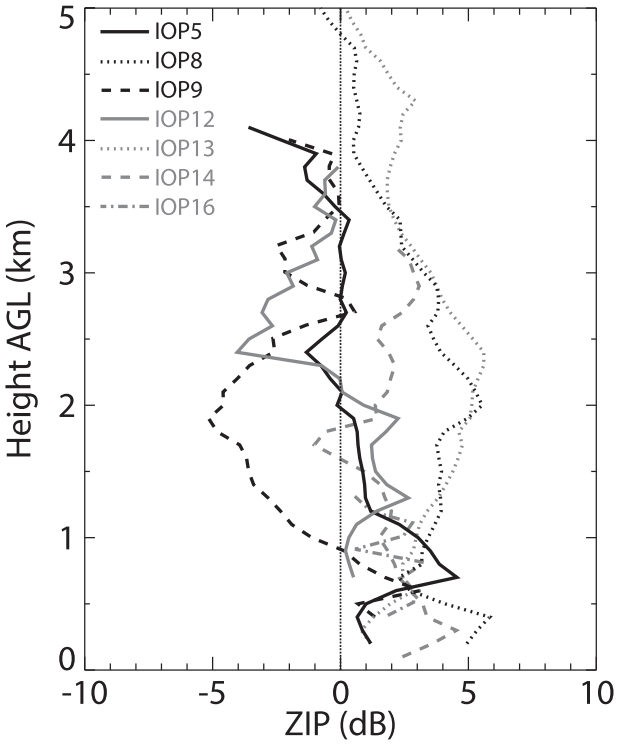

FIG. 8. The ZIP profile for the seven cases, which is defined as the reflectivity change (SEED − NOSEED) in the target region relative to that in the control region.

target regions. We do know that the correlation between the two adjacent regions is high (Fig. 2b). We can further quantify the probability that the observed ZIP values simply are chance occurrences, by computing the probability distribution of double differences derived from random samples of any DOW volume. To do this, we compute the *random double difference* (RDD) as the target-versus-control difference of a random sampling of mean low-level (0–1.5 km AGL) Z (called group A) in comparison with another random sampling of the same (called group B):

$$\mathrm{RDD} = \Delta\mathrm{dB}Z_T - \Delta\mathrm{dB}Z_C, \qquad (2)$$

but here $\Delta\mathrm{dB}Z = \mathrm{dB}Z_A - \mathrm{dB}Z_B$ with the subscripts referring to groups A and B, randomly selected in time (with replacement) from all available DOW volumes, *irrespective of seeding action*. Groups A and B match the durations of the SEED and NOSEED periods. Here, we use the area-mean low-level Z values. We do not randomize in area (the control and target areas are fixed), only in time. For each IOP we repeat this experiment 999 times to obtain a probability distribution of RDD values for each IOP, and the merged RDD probability distribution for all seven IOPs. The latter is shown in Fig. 9a. This distribution is centered near 0.0 dB and is nearly Gaussian; thus, normal statistics can be used. The spread of RDD values is not large for two reasons: the control area correlates well with the target area (Fig. 2b), and the DOW volume interval (10 min) is small compared to the typical advective time scale within the target or control areas. The dotted vertical line in Fig. 9a is the average ZIP value for all IOPs. The mean ZIP is 1.5 dB, which is several standard deviations above the mean, yielding a probability less than 0.1% that the observed SEED − NOSEED difference is by chance.

The value of low-level ZIP is compared with RDD distributions for individual IOPs in Fig. 9b. As expected from Fig. 8, all ZIP values are positive, except for IOP 9. In that case the ZIP is positive near the surface (Fig. 8), but the vertically averaged ZIP (0.2–1.5 km AGL) is negative. In all other IOPs the observed ZIP is at least two standard deviations above the RDD mean values. This significant departure of ZIP from the RDD distribution cannot always be interpreted as a level of confidence in the attribution to seeding. For a normal distribution such as that of RDD, and a ZIP value of, say, three standard deviations above the mean, there is just a 0.1% probability that this ZIP value is obtained by chance. The ZIP value is expected to be large relative to any of the 999 other RDD values, if the reflectivity differences between the two regions continuously increase (or decrease) with time, and if the trend between SEED and NOSEED is large relative to the typical difference between individual samples. In that case, differences in the natural trends between the two regions (even if they are well correlated) can dominate the ZIP value.

To illustrate this, the time series of mean low-level reflectivity in the control and target regions is shown in Fig. 10, for each IOP. Three numbers are shown on the right of each panel. For the entire IOP (NOSEED and SEED), $\Delta\mathrm{dB}Z_T$ and $\Delta\mathrm{dB}Z_C$ are the linear trends in time for the target and control areas, respectively. The third number δZ is the standard deviation of the volume-to-volume differences (i.e., at 10-min intervals). This is an average of two numbers, one for each area (control and target). In some IOPs (e.g., IOPs 5 and 12), the linear trends across the IOP ($\Delta\mathrm{dB}Z_T$ and $\Delta\mathrm{dB}Z_C$) are very different between the two regions and are much larger than the typical volume-to-volume difference. Therefore, the ZIP value includes an unquantifiable natural contribution. Such a natural contribution can be any sign. The fact that the low-level ZIP value is of the same sign in all but one IOP (positive in all seven IOPs if ZIP is averaged over the lowest 1.0 km with data) is the strongest evidence for the attribution to AgI seeding.

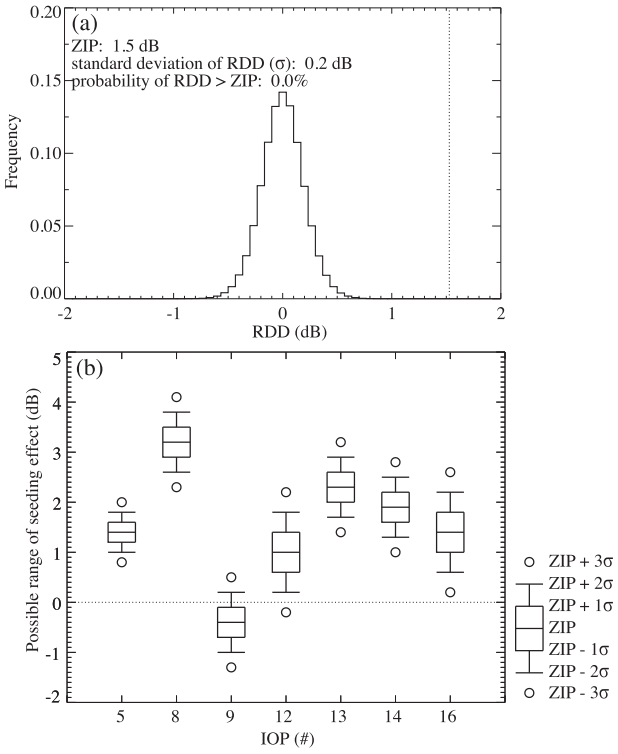

FIG. 9. (a) Composite histograms of low-level RDD values, i.e., possible reflectivity double difference values based on the random sampling of low-level average reflectivity values irrespective of seeding action. The observed mean SEED − NOSEED double difference (ZIP here) is shown by the dotted vertical black line. (b) The ZIP ± 1, 2, and 3 standard deviations of RDD for each IOP.

6. Discussion

The seven cases used in this study constitute the complete array of cases collected in ASCII-12, subject to objective case quality criteria as discussed in section 2b. The IN measurements over the extra-target mountain indicate that ground-released AgI nuclei may be advected over a distance of nearly 100 km across two mountain ranges with a valley in between. The DOW reflectivity data suggest a positive impact of seeding (aimed at the nearby target mountain) on surface precipitation over the foothills of the downwind mountain range, both in the composite and in each of the seven individual cases, at least in the particular case of the mountains in southern Wyoming. Even though all seven cases agree on the sign of the precipitation impact, natural variability cannot be ruled out as a factor, possibly the dominant factor, in the derived ZIP values, as trends in the control area do not need to be the same as in the target area. Attribution to AgI seeding warrants some caution, as has been mentioned in many studies (e.g., Rangno and Hobbs 1995; Garstang et al. 2005; Pokharel et al. 2014b). This study is no exception, especially given its small sample size.

The ambient conditions such as temperature, wind speed, and stability may strongly influence the extra-area seeding effect. For example, high wind speed and low stability may result in strong cross-mountain drift. Previous studies (e.g., Dore and Choularton 1992; Zängl 2008; Zängl et al. 2008; Mott et al. 2014) show the precipitation maxima may shift to the lee area as a result of strong wind drift; thus, more snow particles and possibly more AgI particles could be brought to the lee side. In this study, according to DOW PPI and RHI scans for each IOP (not shown), a precipitation maximum is observed near the crest (<5 km) for the shallow stratiform cases (IOPs 5, 12, and 16). For these cases echoes dissipate quickly on the lee side as a result of the plunging flow (Geerts et al. 2015). The strong wind and downwind drift effect do not shift the precipitation maxima to the lee side. The AgI nuclei could be advected to the Medicine Bow Range by the strong wind, and vertically mixed into clouds through hydraulic jump and PBL mixing, but there is no evidence for enhanced AgI nuclei concentrations in the Medicine Bow Range for the cases with stronger winds. For the shallow convection (IOPs 9 and 14), the plunging flow also results in quick dissipation on the lee side in the Sierra Madre Range, but compared to the stratiform cases, more snow particles, and possibility more AgI nuclei, can be advected to the lee side of the Sierra Madre. The AgI residual in the Medicine Bow Range can be vertically mixed into the clouds through the shallow convection. For the other two deeper cases (IOPs 8 and 13), a precipitation maximum is sometimes observed on the lee side of the Sierra Madre Range, so more snow particles and AgI nuclei may be advected to the Medicine Bow Range as a result of the downwind drift and higher cloud top (thus more time needed for the snow particles to fall to the ground), but we do not have evidence to confirm this hypothesis. The vertical AgI mixing could be deeper as a result of the moderately deep convection and/or a hydraulic jump.

Strong winds may also have an effect on turbulence and vertical air motions (Zängl 2008; Mott et al. 2014). Based on DOW PPI and RHI scans, the clouds on the lee side of the Sierra Madre quickly dissipated for the shallow stratiform cases in this study (IOPs 5, 12, and 16), as a result of plunging flow. There is no evidence to show strong updrafts on the lee side, even though the wind was strong. The updrafts are stronger for the four remaining IOPs studied here, because of a lee hydraulic jump and or convection. A high-resolution profiling Doppler cloud radar can be used in the future to better analyze the effects of wind speed on turbulence and

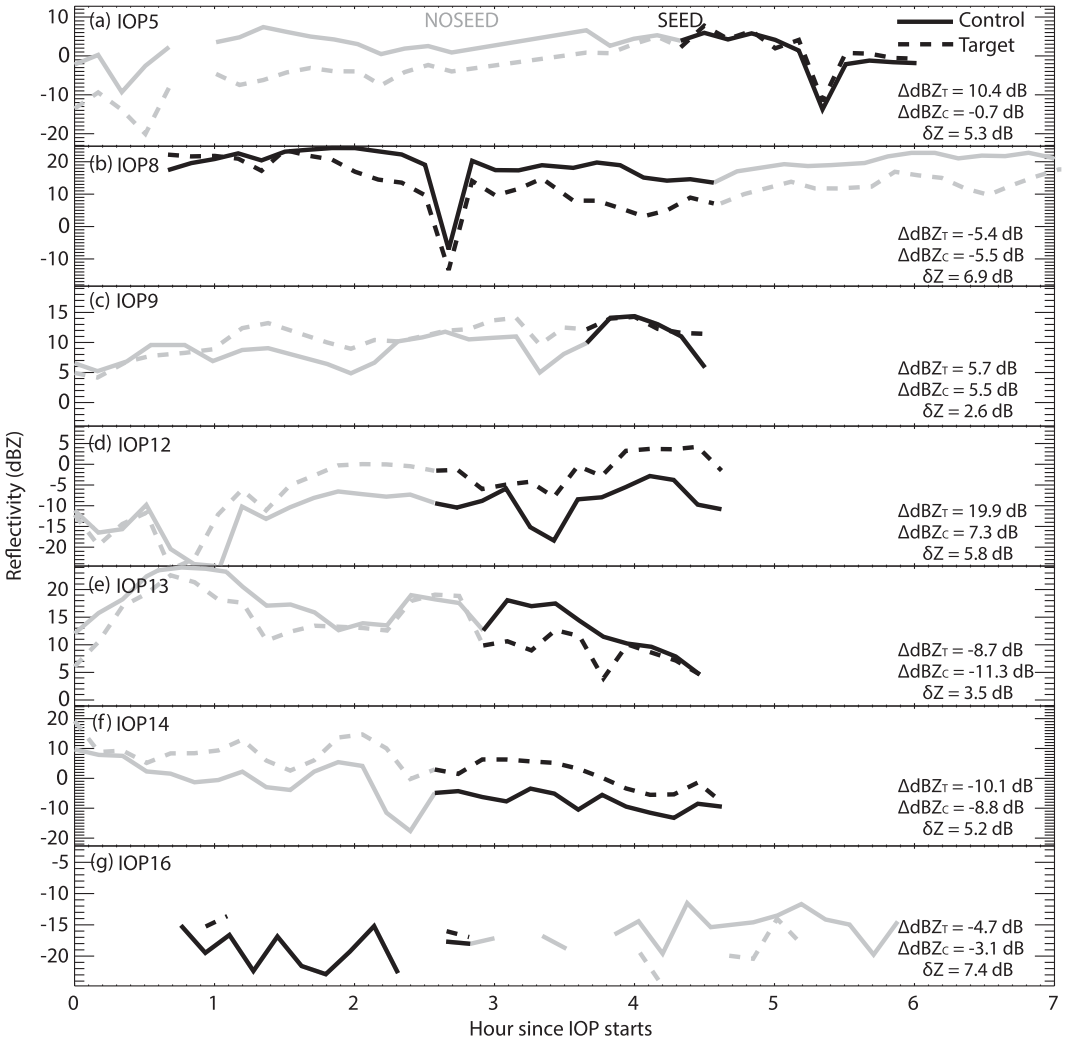

FIG. 10. Time series of low-level area-mean reflectivity for each IOP. Three numbers are shown on the right of each panel: $\Delta\text{dB}Z_T$ and $\Delta\text{dB}Z_C$ are the linear trends in time for the entire IOP (NOSEED and SEED) for the target and control areas, respectively, and δZ is the average standard deviation of the volume-to-volume differences (i.e., at 10-min intervals) for the control and target areas.

vertical air motion (e.g., Geerts et al. 2010), as well as its impact on seeding efficiency.

The natural seeder–feeder mechanism is also important for orographic precipitation and may has an impact on the seeding efficiency. A strong seeder–feeder process can significantly enhance the orographic predication (Zängl 2008; Zängl et al. 2008) and reduce the ground-based seeding efficiency. In this study, all seven of the storms sampled here are rather shallow orographic clouds (Table 2; Fig. 6), so the seeder–feeder mechanism does not apply to this study. Strong low-level flow field may bring more natural ice nuclei from surface to air (blowing snow), but since we are using a lateral control area and a high spatial correlation exists between the two regions (Fig. 2b), the low-level flow and blowing snow impact is expected to be similar in the control and target areas.

Other ambient conditions such as temperature and humidity also may have impacts on extra-area seeding efficiency. For example, less efficient precipitation enhancement in the Sierra Madre Range (e.g., due to high temperature or low humidity) may yield more AgI nuclei over the downwind ranges. Many more cases would be needed to observationally tease out the effects of ambient conditions on extra-area precipitation modification. In fact, the effect of ambient conditions on seeding efficacy in the target area itself (the nearby mountain range, rather than a downwind range) remains difficult to observationally document. A recent study based on all 21 IOPs in ASCII-12 and ASCII-13 using

multiple sensors including the DOW shows that there is no clear relation between ZIP and any single ambient factor, suggesting that seeding efficacy is affected by multiple dynamical and microphysical factors (B. Pokharel et al. 2015, manuscript submitted to *J. Appl. Meteor. Climatol.*). The seeding efficacy appears to be higher on the upwind side (of the target mountain) for stratiform clouds (Jing et al. 2015) and higher on the lee side for convective clouds (Jing and Geerts 2015).

Since the evidence in this study is not conclusive, further observational evidence is needed, as well as further modeling work that can capture the microphysical deposition and long-fetch dispersion of AgI nuclei, and quantify the competing effects of residual AgI nuclei against reduced water vapor availability in storms advected downwind of a seeding target area. Ultimately, a dedicated field campaign is needed, whose experimental design includes not only the target area, but also possible extra-area seeding effects, in order to better understand the impact of seeding on the regional water cycle.

7. Conclusions

This paper examines the possibility of an extra-area seeding effect downwind of the primary target mountain (the Sierra Madre Range), over the foothills of another mountain (the Medicine Bow Range) about 60 km downwind of the AgI generators, using a scanning X-band DOW radar. This radar was deployed on the crest of the Sierra Madre as part of the ASCII-12 campaign and had excellent low-level coverage over the Medicine Bow foothills. All available ASCII-12 IOPs with suitable weather and seeding activities are included in this study. To examine the inadvertent seeding impact, two study areas are designated, both located in the downwind foothills region: a target region centered on the wind direction and an adjacent control region. A comparison is made between the measurements from a treated period (SEED) and those from an untreated period (NOSEED). The findings are as follow:

1) Measurements of IN concentrations show that ground-released AgI nuclei can disperse during winter storms over a distance of nearly 100 km across two mountain ranges.
2) DOW reflectivity difference FADs and mapped reflectivity differences, as well as double precipitation ratio values, indicate a higher precipitation rate in the downwind foothills region directly downwind of the AgI generators during SEED, compared to that in the adjacent control area.
3) In most cases, this positive effect is found at low levels only, but in some cases it is deeper. In those cases DOW RHI scans and echo-height maps, as well as other data collected during ASCII-12, indicate that AgI nuclei may be transported above the well-mixed PBL by convection and/or a hydraulic jump in the lee of the Sierra Madre.
4) The evidence provided here is not conclusive, given the high natural variability of precipitation at fine scales, and the small sample size used in this study (i.e., just seven IOPs and a cumulative 50 h of radar data).

Acknowledgments. The ASCII campaign, including the operation of the DOW, was funded by National Science Foundation Grant AGS-1058426. The DOWs are supported by NSF-1361237. This work also received funding from the Wyoming Water Development Commission and the U.S. Geological Survey, under the auspices of the University of Wyoming Water Research Program. The operation of the AgI generators and microwave radiometer was supported by the Wyoming Weather Modification Pilot Project, which was funded by the State of Wyoming. The dedication of the DOW crew under harsh weather conditions at Battle Pass during ASCII-12 is much appreciated. Binod Pokharel of the University of Wyoming assisted with the processing of sounding data. Katja Friedrich and Joshua Aikins of the University of Colorado assisted with the processing of the DOW data.

REFERENCES

Boe, B. A., J. A. Heimbach, T. W. Krauss, L. Xue, X. Chu, and J. T. McPartland, 2014: The dispersion of silver iodide particles from ground-based generators over complex terrain. Part I: Observations with acoustic ice nucleus counters. *J. Appl. Meteor. Climatol.*, **53**, 1325–1341, doi:10.1175/JAMC-D-13-0240.1.

Breed, D., R. Rasmussen, C. Weeks, B. Boe, and T. Deshler, 2014: Evaluating winter orographic cloud seeding: Design of the Wyoming Weather Modification Pilot Project (WWMPP). *J. Appl. Meteor. Climatol.*, **53**, 282–299, doi:10.1175/JAMC-D-13-0128.1.

Chu, X., L. Xue, B. Geerts, R. Rasmussen, and D. Breed, 2014: A case study of radar observations and WRF LES simulations of the impact of ground-based glaciogenic seeding on orographic clouds and precipitation. Part I: Observations and model validations. *J. Appl. Meteor. Climatol.*, **53**, 2264–2286, doi:10.1175/JAMC-D-14-0017.1.

DeFelice, T. P., J. Golden, D. Griffith, W. Woodley, D. Rosenfeld, D. Breed, M. Solak, and B. Boe, 2014: Extra-area effects of cloud seeding: An updated assessment. *Atmos. Res.*, **135–136**, 193–203, doi:10.1016/j.atmosres.2013.08.014.

DeMott, P. J., 1997: Report to North Dakota Atmospheric Resource Board and Weather Modification Incorporated on tests of the ice nucleating ability of aerosols produced by the Lohse airborne generator. 15 pp [Report available from the Dept. of Atmospheric Science, Colorado State University, 3915 W. Laport Ave., Fort Collins, CO 80523.]

Dore, A. J., and T. W. Choularton, 1992: Orographic enhancement of snowfall. *Environ. Pollut.*, **75**, 175–179, doi:10.1016/0269-7491(92)90037-B.

Gabriel, K. R., 1999: Ratio statistics for randomized experiments in precipitation stimulation. *J. Appl. Meteor.*, **38**, 290–301, doi:10.1175/1520-0450(1999)038<0290:RSFREI>2.0.CO;2.

Garstang, M., R. Bruintjes, R. Serafin, H. Orville, B. Boe, W. Cotton, and J. Warburton, 2005: Finding common ground. *Bull. Amer. Meteor. Soc.*, **86**, 647–655, doi:10.1175/BAMS-86-5-647.

Geerts, B., Q. Miao, Y. Yang, R. Rasmussen, and D. Breed, 2010: An airborne profiling radar study of the impact of glaciogenic cloud seeding on snowfall from winter orographic clouds. *J. Atmos. Sci.*, **67**, 3286–3301, doi:10.1175/2010JAS3496.1.

——, and Coauthors, 2013: The AgI Seeding Cloud Impact Investigation (ASCII) campaign 2012: Overview and preliminary results. *J. Wea. Modif.*, **45**, 24–43.

——, Y. Yang, R. Rasmussen, S. Haimov, and B. Pokharel, 2015: Snow growth and transport patterns in orographic storms as estimated from airborne vertical-plane dual-Doppler radar data. *Mon. Wea. Rev.*, **143**, 644–665, doi:10.1175/MWR-D-14-00199.1.

Griffith, D. A., M. E. Solak, R. D. Almy, and D. Gibbs, 2005: The Santa Barbara Cloud Seeding Project in Southern California, summary of results and their implications. *J. Wea. Modif.*, **37**, 21–27.

——, ——, and D. P. Yorty, 2009: 30+ seasons of operational cloud seeding in Utah. *J. Wea. Modif.*, **41**, 23–37.

Hashimoto, A., T. Kato, S. Hayashi, and M. Murakami, 2008: Seedability assessment for winter orographic snow clouds over the Echigo Mountains. *SOLA*, **4**, 69–72, doi:10.2151/sola.2008-018.

Holroyd, E. W., J. T. McPartland, and A. B. Super, 1988: Observation of silver iodide plumes over the Grand Mesa of Colorado. *J. Appl. Meteor.*, **27**, 1125–1144, doi:10.1175/1520-0450(1988)027<1125:OOSIPO>2.0.CO;2.

Huggins, A. W., 2007: Another wintertime cloud seeding case study with strong evidence of seeding effects. *J. Wea. Modif.*, **39**, 9–36. [Available online at http://www.weathermodification.org/publications/index.php/JWM/article/view/195.]

Hunter, S., 2009: Comprehensive literature survey on the potential extra-area precipitation effects of winter cloud seeding. Colorado Water Conservation Board Tech. Rep., 48 pp. [Available online at http://cwcb.state.co.us/.]

Jing, X., and B. Geerts, 2015: Dual-polarization radar data analysis of the impact of ground-based glaciogenic seeding on winter orographic clouds. Part II: Convective clouds. *J. Appl. Meteor. Climatol.*, **54**, 2099–2117, doi:10.1175/JAMC-D-15-0056.1.

——, ——, K. Friedrich, and B. Pokharel, 2015: Dual-polarization radar data analysis of the impact of ground-based glaciogenic seeding on winter orographic clouds. Part I: Mostly stratiform clouds. *J. Appl. Meteor. Climatol.*, **54**, 1944–1969, doi:10.1175/JAMC-D-14-0257.1.

Long, A. B., 2001: Review of downwind extra-area effects of precipitation enhancement. *J. Weather Modif.*, **33**, 24–45.

Manton, M. J., L. Warren, S. L. Kenyon, A. D. Peace, S. P. Bilish, and K. Kemsley, 2011: A confirmatory snowfall enhancement project in the Snowy Mountains of Australia. Part I: Project design and response variables. *J. Appl. Meteor. Climatol.*, **50**, 1432–1447, doi:10.1175/2011JAMC2659.1.

Matrosov, S. Y., C. Campbell, D. Kingsmill, and E. Sukovich, 2009: Assessing snowfall rates from X-band radar reflectivity measurements. *J. Atmos. Oceanic Technol.*, **26**, 2324–2339, doi:10.1175/2009JTECHA1238.1.

Mott, R., D. Scipión, M. Schneebeli, N. Dawes, A. Berne, and M. Lehning, 2014: Orographic effects on snow deposition patterns in mountainous terrain. *J. Geophys. Res. Atmos.*, **119**, 1363–1385, doi:10.1002/2013JD019880.

Mulvey, G. J., 1977: Physical mechanisms of extra area effects from weather modification. Ph.D. dissertation, Colorado State University, 155 pp.

Pokharel, B., B. Geerts, and X. Jing, 2014a: The impact of ground-based glaciogenic seeding on orographic clouds and precipitation: A multisensor case study. *J. Appl. Meteor. Climatol.*, **53**, 890–909, doi:10.1175/JAMC-D-13-0290.1.

——, and Coauthors, 2014b: The impact of ground-based glaciogenic seeding on clouds and precipitation over mountains: A multisensor case study of shallow precipitating orographic cumuli. *Atmos. Res.*, **147–148**, 162–182, doi:10.1016/j.atmosres.2014.05.014.

——, B. Geerts, and X. Jing, 2015: The impact of ground-based glaciogenic seeding on clouds and precipitation over mountains: a case study of a shallow orographic cloud with large supercooled droplets. *J. Geophys. Res. Atmos.*, **120**, 6056–6079, doi:10.1002/2014JD022693.

Rangno, A. L., and P. V. Hobbs, 1995: A new look at the Israeli cloud seeding experiments. *J. Appl. Meteor.*, **34**, 1169–1193, doi:10.1175/1520-0450(1995)034<1169:ANLATI>2.0.CO;2.

Solak, M. E., D. P. Yorty, and D. A. Griffith, 2003: Estimations of downwind cloud seeding effects in Utah. *J. Wea. Modif.*, **35**, 52–58.

Wise, E. A., 2005: Precipitation evaluation of the North Dakota Cloud Modification Project (NDCMP). M.S. thesis, Dept. of Atmospheric Science, University North Dakota, Grand Forks, ND, 63 pp.

Wyoming Water Development Commission, 2014: The Wyoming Weather Modification Pilot Project Executive Summary. Wyoming Water Development Commission, Cheyenne, WY, 16 pp. [Available online at http://wwdc.state.wy.us/weathermod/WYWeatherModPilotProgramExecSummary.html or from Wyoming Water Development Commission, 6920 Yellowtail Rd., Cheyenne, WY 82009.]

Xue, L., X. Chu, R. Rasmussen, D. Breed, B. Boe, and B. Geerts, 2014: The dispersion of silver iodide particles from ground-based generators over complex terrain. Part II: WRF large-eddy simulations versus observations. *J. Appl. Meteor. Climatol.*, **53**, 1342–1361, doi:10.1175/JAMC-D-13-0241.1.

Yuter, S. E., and R. A. Houze Jr., 1995: Three-dimensional kinematic and microphysical evolution of Florida cumulonimbus. Part II: Frequency distributions of vertical velocity, reflectivity, and differential reflectivity. *Mon. Wea. Rev.*, **123**, 1941–1963, doi:10.1175/1520-0493(1995)123<1941:TDKAME>2.0.CO;2.

Zängl, G., 2008: The temperature dependence of small-scale orographic precipitation enhancement. *Quart. J. Roy. Meteor. Soc.*, **134**, 1167–1181, doi:10.1002/qj.267.

——, D. Aulehner, C. Wastl, and A. Pfeiffer, 2008: Small-scale precipitation variability in the Alps: Climatology in comparison with semi-idealized numerical simulations. *Quart. J. Roy. Meteor. Soc.*, **134**, 1865–1880, doi:10.1002/qj.311.